Monthly Notices of the ROYAL ASTRONOMICAL SOCIETY

MNRAS **546,** 1–8 (2026) https://doi.org/10.1093/mnras/stag154
Advance Access publication 2026 January 23

The relationship between accretion and ionized ejection among young stellar objects in the Coronet cluster

Arpan Ghosh [1]★ Roberto Galván-Madrid [1] Johanan Ramírez-Arellano,[1] Carlos Carrasco-González [1] Gráinne Costigan [2] Suzanne Ramsay [3] Carlo Manara [3] Jan Forbrich [4] Hauyu Baobab Liu [5,6] and Michihiro Takami [7]

[1]*Universidad Nacional Autónoma de México, Instituto de Radioastronomía y Astrofísica, 58090 Morelia, Michoacán, México*
[2]*Grünenthal GmbH, Aachen, Germany*
[3]*European Southern Observatory, Karl-Schwarzschild-Strasse 2, D-85748 Garching bei München, Germany*
[4]*Centre for Astrophysics Research, University of Hertfordshire, College Lane, Hatfield AL10 9AB, UK*
[5]*Department of Physics, National Sun Yat-Sen University, No. 70, Lien-Hai Road, Kaohsiung City 80424, Taiwan, R.O.C.*
[6]*Center of Astronomy and Gravitation, National Taiwan Normal University, Taipei 116, Taiwan, R.O.C.*
[7]*Institute of Astronomy and Astrophysics, Academia Sinica, 11F Astronomy-Mathematics Building, No.1, Section 4, Roosevelt Rd, Taipei 10617, Taiwan, R.O.C.*

Accepted 2026 January 16. Received 2026 January 16; in original form 2025 October 10

ABSTRACT

We present results from a coordinated, multi-epoch near-infrared and centimetre radio survey of young stellar objects (YSOs) in the Coronet, aimed at probing the connection between mass accretion and ionised mass-loss. Using VLT-KMOS, we detect Brγ emission in 5 of the 26 targets, which also exhibit 3.3-cm continuum emission in VLA images, consistent with partially ionised jets. For seven additional sources, stringent flux upper limits were obtained. The derived accretion and ionized mass-loss rates for class I and class II YSOs follow a sublinear correlation $\dot{M}_{\rm ion} \propto \dot{M}_{\rm acc}^{0.3}$, consistent with previous results for class II YSOs but extended here to earlier stages. Multi-epoch observations reveal modest variability in both tracers but no clear temporal correlation between accretion and ejection within time-scales of a few months. The ratio $\dot{M}_{\rm ion}/\dot{M}_{\rm acc}$ shows an anticorrelation with $\dot{M}_{\rm acc}$, increasing with time from class I YSOs to class II YSOs, suggesting an increase in jet-launching efficiency or ionization fraction with evolution. These findings support a direct connection between accretion and outflow across the $\sim$ Myr time-scale of YSO evolution, while highlighting the complexity of their short-term interplay.

Key words: stars: activity – circumstellar matter – stars : evolution – stars : formation – stars : magnetic field.

1 INTRODUCTION

The mass assembly during star formation occurs through the accretion of material from a circumstellar disk to the central object (L. Hartmann, G. Herczeg & N. Calvet 2016). During the earliest class 0 and I stages of Young Stellar Object evolution (YSO, F. C. Adams, C. J. Lada & F. H. Shu 1987; P. Andre, D. Ward-Thompson & M. Barsony 1993), the protostars and their discs are also surrounded by dense envelopes, which are cleared out within a Myr (M. M. Dunham et al. 2014). The later YSO stages (class II and III) are marked by the evolution of their discs, with a gradual decline in their gas content and accretion rates over a few Myr (P. J. Armitage, C. J. Clarke & F. Palla 2003; J. P. Williams & L. A. Cieza 2011; C. F. Manara et al. 2023; E. Gaidos, L. Gehrig & M. Güdel 2025).

A fraction of the accreted material is ejected in the form of jets and disc-winds, which are crucial for the release of specific angular momentum, as well as for disc dispersal (A. Frank et al. 2014; I. Pascucci et al. 2023). In standard theoretical models, the ejection and accretion of material are coupled through magnetohydrodynamical (MHD) processes (F. Shu et al. 1994; R. E. Pudritz et al. 2007). Therefore, a common expectation is that accretion and ejection will be coupled in time. However, detailed theoretical modelling of these processes across YSO evolution is challenging (e.g. M. M. Romanova et al. 2018; Z. Zhu 2025). Furthermore, YSOs show evidence of time variability within time-scales much shorter than their evolutionary time-scale in their accretion rates, ejected jets, and circumstellar material (e.g. M. Morales-Calderón et al. 2011; W. J. Fischer et al. 2023; V. Lora et al. 2024).

A joint characterization of accretion and ejection processes across YSO evolutionary types requires multiwavelength data. Emission of hydrogen (H I) recombination lines such as Brγ, emitted in the accretion shock around the stellar surface, have become the standard to measure accretion (D. F. M. Folha & J. P. Emerson 2001; J. Muzerolle, N. Calvet & L. Hartmann 2001). In the least embedded YSOs, jets and disc-winds are commonly studied via optical lines, e.g. [O I] (P. Hartigan, S. Edwards & L. Ghandour 1995; M. Fang et al. 2018; B. Nisini et al. 2018; A. Banzatti et al. 2019), as well as with near-infrared molecular hydrogen

★ E-mail: a.ghosh@irya.unam.mx(AG); 19aghosh91@gmail.com(AG)

H_2 emission (M. Takami et al. 2006; C. Contreras Peña et al. 2017; Z. Guo et al. 2020). Radio continuum emission at centimetre wavelengths is known to be an effective tracer of the partially ionized base of jets (L. F. Rodríguez et al. 2014; G. Anglada, L. F. Rodríguez & C. Carrasco-González 2018). This tracer is particularly valuable in the more embedded class 0/I YSOs (Ł. Tychoniec et al. 2018). However, other physical processes can contribute to the observed centimetre emission. Non-thermal (gyro)synchrotron emission from an active stellar magnetosphere is expected to dominate in class IIIs and could contaminate the emission of less evolved YSOs (e.g. H. B. Liu et al. 2014; J. Forbrich et al. 2021).

In this paper, we report the results of a coordinated monitoring of YSOs in the R Corona Australis (R CrA) star forming region, using Brγ and centimetre continuum as tracers of accretion and ejection, respectively. Recent studies by A. A. Rota et al. (2024, 2025) and A. Garufi et al. (2025) have explored the relationship between accretion and ejection using these tracers, but they have focused on class II YSOs, and their observations were not quasi-simultaneous. The *Coronet* cluster in R CrA is an excellent target because it is nearby (152 pc; P. A. B. Galli et al. 2020, see also S. A. Dzib et al. 2018) and remains embedded in its natal cloud (A. Sicilia-Aguilar et al. 2011), hosting a large concentration of YSOs at different evolutionary stages (B. Nisini et al. 2005a; A. Sicilia-Aguilar et al. 2008; P. C. Myers 2009; D. E. Peterson et al. 2011; P. Cazzoletti et al. 2019). The Coronet has also been studied in the radio continuum (M. Choi et al. 2008; O. Miettinen et al. 2008; H. B. Liu et al. 2014), including monitoring campaigns with X-ray observations (J. Forbrich et al. 2007).

The paper is arranged as follows. Section 2 describes the observations and data analysis, followed by the results in Section 3. The implications of our results are discussed in Section 4, and Section 5 presents our conclusions.

2 OBSERVATIONS AND DATA ANALYSIS

2.1 Near-infrared data

We have selected a sample of 26 YSOs within the Coronet cluster, spanning the evolutionary range from class I to class III. The YSOs were selected from those reported by D. E. Peterson et al. (2011) in their study using *Spitzer*. The selected YSOs were observed with the *K*-band Multi Object Spectrograph (KMOS; R. Sharples et al. 2013) on the Very Large Telescope (VLT), using the *K*-band set-up, which provides a wavelength coverage between 1.934 and 2.460 μm at a resolution of $R \sim 4200$. The observations were carried out between April 27 and July 22, 2014, as part of proposal ID 093.C-0657 (P.I. Galván-Madrid). The target-of-opportunity (ToO) mode was used, triggered by observations taken with the Very Large Array. The data were reduced using the KMOS version 2.7.3 pipeline within ESOReflex (R. I. Davies et al. 2013; W. Freudling et al. 2013). The 1D spectrum was extracted by averaging over a 10×10 pixel region of the spatial axes centred on the source peak, chosen to maximize the S/N and ensure uniform aperture losses across epochs with varying seeing conditions. For epochs where the source was not well centred within the IFU field of view, a smaller region was adopted. The spatially integrated spectra from the output KMOS data cubes were calibrated using photometry obtained from the 2MASS (M. F. Skrutskie et al. 2006) and VISIONS (S. Meingast et al. 2023) surveys. In a way similar to E. Fiorellino et al. (2021), this latter procedure was adopted to improve the spectro-photometry of the original KMOS data.

2.2 Radio data

Observations were conducted with the NRAO's Karl G. Jansky Very Large Array (VLA). Partial results of the monitoring programme, which ran from 2012 to 2015, have been published in H. B. Liu et al. (2014) and R. Galván-Madrid et al. (2014). The full results will be presented in Ramírez-Arellano et al. (in preparation) During the months of the KMOS programme, the VLA observed for ten epochs: seven in the X band (3.3 cm) and three in the Ku band (2.1 cm). In this paper, we make use of the higher quality X-band data from those epochs, as well as the image created by concatenating the visibilities of 32 X-band epochs from the entire program.

The VLA observations were carried out in single-pointing mode, centered at $\alpha(\mathrm{J2000}) = 19^h\ 01^m\ 48.0^s$, $\delta(\mathrm{J2000}) = -36^\circ\ 57'\ 59.00''$. Data were calibrated using the Common Astronomy Software Applications package, version 6.5.4 (CASA Team 2022). Standard calibration and imaging steps were followed (see H. B. Liu et al. 2014). The phases of the visibilities in each epoch were self-calibrated, and individual-epoch images were created with these. Also, deep images were made from the concatenated visibilities of all epochs. All the images used in this paper were produced using the `tclean` task within `CASA`, utilizing *Briggs* weighting with robust = 0. The central frequency of the images is 9.0 GHz (3.3 cm).

The most sensitive image is the one created with the concatenated visibilities. The rms noise prior to the correction of the primary-beam response is 9 μJy beam^{-1}. The FWHM beamsize of this image is $\theta_{\mathrm{maj}} \times \theta_{\mathrm{min}} = 1.85$ arcsec $\times$ 0.78 arcsec, with a position angle (P.A.) = 4.2°.

2.3 Flux measurements

We inspected the flux-calibrated, spatially averaged KMOS spectra of each epoch, looking for the Brγ line at 2.166 μm. We detected Brγ in seven out of the 26 targeted YSOs. Among them, the line was found to be in emission in five YSOs and in absorption in the remaining two (see Table 1). To measure the Brγ fluxes, we fitted a model that includes a Gaussian for the Brγ line and a first-order polynomial for the adjacent continuum. For this, we used the `LevMarLSQFitter` within the `astropy` modeling package (Astropy Collaboration 2022). The line flux was measured as the area under the fitted Gaussian, along with the corresponding error propagation. This procedure was performed for the individual epochs and for the median-combined spectrum of each source. Of the remaining 19 targets, two (JVLA4 and Peterson4) had no detectable continuum within the IFU field of view, one (CrA19) had a coordinate mismatch with the radio data, and two with extended radio emission (IRS7E and IRS7W) were excluded. The remaining 14 sources show no Brγ detection. These comprise seven class III, six class II, and one class I YSOs. The 1D spectra of the seven class II and class I sources from individual epochs were averaged and combined to produce a single spectrum. The upper limit on their Brγ flux was then estimated following the procedure of E. Fiorellino et al. (2021), modified as follows:

$$F_{\mathrm{upper}} = 3 \times \sigma_{\mathrm{rms}} \times \sqrt{N_{\mathrm{chan}}} \times \Delta v, \quad (1)$$

where N_{chan} corresponds to the number of channels across the line width, given by $\lambda_{\mathrm{line}}/R$, with λ_{line} as the central Brγ wavelength, R the KMOS *K*-band resolution, and Δv as the channel spacing.

Table 1. Summary of the parameters of the Brγ detected sources. Sources with upper limits in both Brγ and 3.3 cm are labelled 'Ul'.

Source	RA (J2000)	Dec. (J2000)	YSO Class	Brγ	3.3cm Radio	Mass ($M_\odot$)	Radius ($R_\odot$)	A_V (mag)
IRS1	19:01:50.705	−36:58:09.55	I	Em	Yes	0.40	6.00	30.0
IRS2	19:01:41.582	−36:58:31.07	I	Em	Yes	1.40	2.90	20.0
CrA43	19:01:58.564	−36:57:08.23	I	Em	Yes	3.54	2.32	16.5
IRS6	19:01:50.480	−36:56:37.90	II	Abs	Yes	0.20	2.32	29.0
TCrA	19:01:58.784	−36:57:49.78	II	Em	Yes	2.25	1.14	2.5
CrA16	19:01:33.877	−36:57:44.71	II	Em	Yes	0.32	1.22	16.6
JVLA1	19:01:34.917	−37:00:56.84	III	Abs	Yes	1.34	1.94	1.4
CrA26	19:02:06.833	−36:58:41.43	II	Ul	Ul	0.18	2.10	1.2
Peterson1	19:01:32.345	−36:58:02.97	II	Ul	Ul	0.28	1.21	14.7
Peterson6	19:01:53.775	−37:00:33.80	II	Ul	Ul	0.10	0.47	0.2
IRS10	19:02:04.109	−36:57:00.72	II	Ul	Ul	0.16	1.68	9.76

Note. Stellar parameters are from B. Nisini et al. (2005b) and R. Dong, J. R. Najita & S. Brittain (2018). For CrA43, Peterson1, Peterson6, IRS10, and CrA26, parameters were obtained from SED fitting using `SEDFITTER` (T. P. Robitaille et al. 2007).

VLA data obtained nearly simultaneously[1] with the KMOS observations were used to investigate temporal correlations between the two. Photometry in the radio images was obtained using the `imfit` task within `CASA`, which performs Gaussian fitting of the source emission, including error estimation. We take the fitted peak intensity as the source flux. This ensures that the radio flux corresponds to the same arcsecond scale as the KMOS IFU measurement. Also, time-averaged photometry was obtained from the `imfit` results in the concatenated image and from averaging the results in the individual epochs matching the KMOS program (see Section 2.2).

3 RESULTS

3.1 Relationship between Brγ and 3.3 cm radio fluxes

Table 1 lists the Brγ and radio detections of the YSOs. In the per-epoch images, the radio continuum emission from CrA16 was not detected. However,in the concatenated radio image, this source has a detection at $\approx 94 \pm 21$ μ Jy beam^{-1}. The rest of the Brγ detected radio sources are detected both in the concatenated image and in individual epochs. Among the YSOs, only JVLA1 and IRS6 have Brγ in absorption, whereas in the rest of the detections, the line is in emission. IRS6 is a binary system, and the component designated as IRS6a is the only one with detectable spectral features (B. Nisini et al. 2005a). In this paper, references to IRS6 specifically denote the IRS6a component. The Brγ absorption line profile of IRS6 is not very wide; hence, we refrain from inferring further about the observed profile. JVLA1 is a class III YSO with a K1 IV subgiant spectral type (J. Forbrich & T. Preibisch 2007). The KMOS spectrum of JVLA1 has prominent absorption features in Brγ and the CO (2–0) and (3–1) bandheads. A. Sicilia-Aguilar et al. (2011) reported minimal infrared excess in JVLA1. Therefore, the absorption lines of JVLA1 likely originate from a cool photosphere.

The time-averaged Brγ and 3.3 cm fluxes in our sample are shown in Fig. 1. We have used the Brγ fluxes averaged over all the observation epochs and the radio fluxes from the concatenated image at 3.3 cm. We have employed a Markov Chain Monte Carlo (MCMC) method for the Bayesian linear regression since it is well suited for data sets containing measurements with uncertainties in both variables. A linear fit to the data gives the following shallow, positive relation:[2] $\log(F_{3.3\,\mathrm{cm}}) = (4.3 \pm 2.1) + (0.29 \pm 0.12) \times \log(F_{Br\gamma})$. As we will see in the following, a correlation between these two tracers is not expected for all YSO types.

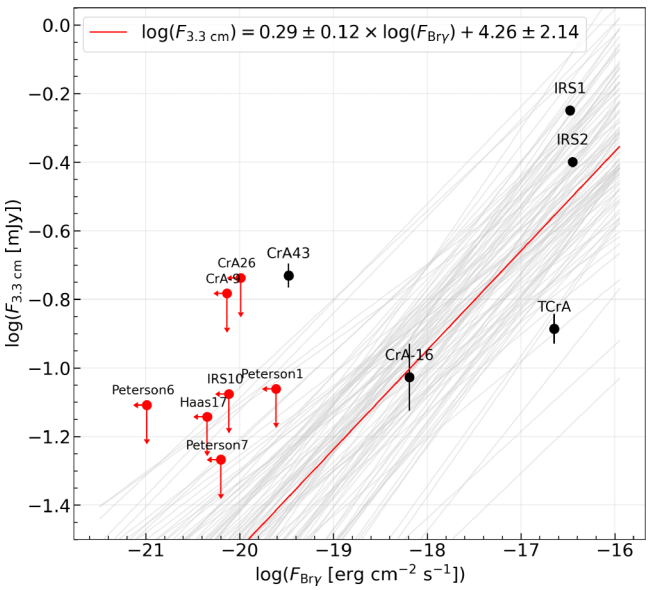

Figure 1. Relationship between the Brγ and the 3.3 cm radio continuum fluxes for the class I and II sources. Detected sources are denoted by black symbols and upper limits by red symbols. Grey curves illustrate posterior regression lines consistent with the 68 per cent credible interval of the slope; the median relation is shown in red.

In the standard scenario of disk evolution, accretion rates are expected to decrease significantly from the class I to the class II YSO stages (L. Hartmann et al. 2016). Consequently, if the centimetre free–free emission from YSOs is caused mainly by

[1]Since the VLT and VLA epochs were not observed at the exact same time, we consider observations separated by up to ten days as near-simultaneous.

[2]Throughout the rest of this paper, radio continuum fluxes are in units of millijansky (mJy), and Brγ fluxes are in units of erg s^{-1} cm^{-2}.

partially-ionised jets (G. Anglada et al. 2018), and if the strength of those jets is linked to that of accretion, a relationship between Brγ and radio continuum is expected. This has been recently reported for class II YSOs (A. A. Rota et al. 2024; A. Garufi et al. 2025), including transition disks (A. A. Rota et al. 2025). However, the faint centimetre continuum from class II YSOs could also be due to disk photo-evaporation by EUV photons (R. Galván-Madrid et al. 2014; I. Pascucci et al. 2014; E. Macías et al. 2016), which could nevertheless be linked to accretion in a complex way via disc winds (I. Pascucci et al. 2023). In the class III stage, where the magnetosphere of the un-embedded young star becomes exposed, centimetre radio emission can become bright again, highly variable, and non-thermal in nature (H. B. Liu et al. 2014; J. Forbrich et al. 2021). This non-thermal radio emission is not expected to be correlated with accretion phenomena. It is worth mentioning that class 0/I YSOs also exhibit non-thermal radio emission; however, only a few have been observed, e.g. IRS 5 in the Coronet cluster (E. D. Feigelson & T. Montmerle 1999; A. T. Deller, J. Forbrich & L. Loinard 2013; H. B. Liu et al. 2014). Such emission is typically identified through circular polarization; however, it is expected that in the majority of younger YSOs non-thermal emission is easily veiled by the free–free component along the line of sight (P. Andre 1987; A. T. Deller et al. 2013).

3.2 Relationship between accretion and ionised mass-loss rates

Brγ fluxes were converted to the corresponding mass accretion rates ($\dot{M}_{\rm acc}$) using the relations of J. M. Alcalá et al. (2017). Although these relations were calibrated for class II YSOs, we also apply them to class I YSOs, assuming that the underlying accretion engine in class I protostars is similar to that of more evolved class II systems, as supported by recent studies (e.g. Fiorellino et al. 2023; L. Testi et al. 2025). The stellar parameters of mass (M_*), radius (R_*), and extinction (A_V) are summarized in Table 1. The conversion was carried out for five class I and II sources with Brγ detections and for three of the seven upper-limit YSOs with available photometry from VISIONS and *Spitzer*/*WISE*. The Brγ fluxes of the YSOs have been extinction corrected with corresponding A_V values using the relation given in J. M. Alcalá et al. (2017) and uncertainties in the fluxes, stellar masses, and radii were propagated into the accretion-rate estimates. Since class I YSOs have significant veiling[3] in their spectra, we have followed the recipe described by E. Fiorellino et al. (2021) to correct for this veiling in our three class I sources; accretion rates were computed over the allowed range of veiling values and combined to derive weighted mean $\dot{M}_{\rm acc}$ estimates.

The 3.3 cm radio continuum fluxes are transformed to ionized mass-loss rates ($\dot{M}_{\rm ion}$) for the eight class I and II YSOs with an accretion rate measurement or upper limit (see Table 1 in the online supplementary material). Five of them are VLA detections (IRS1, IRS2, CrA43, TCrA, CrA16). For CrA26, Peterson 1, and Peterson 6 we use 3σ from the local noise in the VLA image. The class III YSO JVLA1 has been excluded because the jet interpretation is not appropriate for the radio continuum of the more evolved YSOs (see Section 3.1). We follow equation (11) of G. Anglada et al. (2018), assuming a conical jet geometry. Disc inclination angles (i) for IRS1, IRS2, TCrA, CrA16, and CrA43 are obtained from P. Cazzoletti et al. (2019) and C.-H. Hsieh et al. (2024). For sources lacking inclination information, we assume $i = 60^{\circ}$, corresponding to the median inclination angle expected for a randomly oriented sample. Following A. A. Rota et al. (2024), we assume the jet to be perpendicular to the disk plane and therefore aligned with the inclination of the outer disk. The jet velocity ($v_{\rm jet}$) is estimated from the stellar mass M_* using equation (12) of G. Anglada et al. (2018). We conduct this analysis for both the epoch-averaged data and the individual epoch detections. The errors in the mass rates were estimated using the `uncertainties` [4] PYTHON package, propagating from the errors in the measured fluxes, disk inclination, jet angular size, jet velocity and electron temperature.

Fig.2 presents the temporal evolution of $\dot{M}_{\rm acc}$ and $\dot{M}_{\rm ion}$ for the three YSOs with individual-epoch measurements. CrA43, although detected in individual epochs, is excluded from further analysis because its derived $\dot{M}_{\rm ion}$ is unphysically larger than $\dot{M}_{\rm acc}$ (see Section 4.3). The three analysed objects, IRS1, IRS2, and TCrA, exhibit variability of 0.12, 0.27, and 0.17 dex, respectively, from their mean rates. No apparent correlation in time is seen between these two quantities, suggesting that a larger temporal coverage is needed (e.g. M. Takami et al. 2020).

For the time-averaged values, we performed Bayesian linear regression fits to the logarithm of $\dot{M}_{\rm ion}$ as a function of the logarithm of $\dot{M}_{\rm acc}$ under two conditions: (i) taking the Brγ fluxes from the fits to the averaged spectra and the 3.3 cm fluxes from the epoch-concatenated VLA image (see Figs 1 and 2 of the online supplementary material) and (ii) from averaging the $\dot{M}_{\rm acc}$ and $\dot{M}_{\rm ion}$ values of the near-simultaneous epochs, as shown in Fig. 2, but taking the 3.3 cm flux of CrA16 from the concatenated image and the upper limit fluxes of Peterson 1, Peterson 6, and CrA26 from the concatenated centimetre image and Brγ spectra. Based on the expected physical connection between $\dot{M}_{\rm ion}$ and $\dot{M}_{\rm acc}$, we assume flat bounded priors on the slope (0–2) and intercept (−10 to 10). Fig. 3 shows the $\dot{M}_{\rm acc}$ and $\dot{M}_{\rm ion}$ values and fits for these two cases. We also converted the 3.3 cm fluxes at lower angular resolution reported in H. B. Liu et al. (2014) into the corresponding $\dot{M}_{\rm ion}$, and overplotted them in Fig. 3, using accretion rates from B. Nisini et al. (2005a).

The obtained fits to our data are $\log(\dot{M}_{\rm ion}) = (-7.1 \pm 0.8) + (0.26 \pm 0.13) \times \log(\dot{M}_{\rm acc})$ for case i, and $\log(\dot{M}_{\rm ion}) = (-7.1 \pm 0.8) + (0.27 \pm 0.14) \times \log(\dot{M}_{\rm acc})$ for case ii. This analysis aimed to assess the impact of temporal variability in our coordinated observations, as YSOs can display short time-scale behaviour (e.g. dipper or burster variability) capable of significantly affecting the inferred relationships. The observed variations in $\dot{M}_{\rm ion}$ and $\dot{M}_{\rm acc}$ across the monitoring epochs were modest of the order of ~ 0.1 dex, and do not affect the resulting slope of the relation.

4 DISCUSSION

4.1 Ionized ejection with respect to accretion

Fig.4 shows an anti-correlation between the logarithmic ratio $\dot{M}_{\rm ion}/\dot{M}_{\rm acc}$ as a function of the logarithm of $\dot{M}_{\rm acc}$. A linear fit gives $\log(\dot{M}_{\rm ion}/\dot{M}_{\rm acc}) = (-7.6 \pm 1.7) - (0.84 \pm 0.29) \times \log(\dot{M}_{\rm acc})$.

Considering that $\dot{M}_{\rm ejection}/\dot{M}_{\rm acc}$ probes the efficiency ξ of the ejection process compared to that accreted by the protostar, in

[3] Veiling refers to the excess continuum emission arising from the circumstellar disc due to the accretion process (e.g. N. Calvet & E. Gullbring 1998).

[4] https://pypi.org/project/uncertainties/

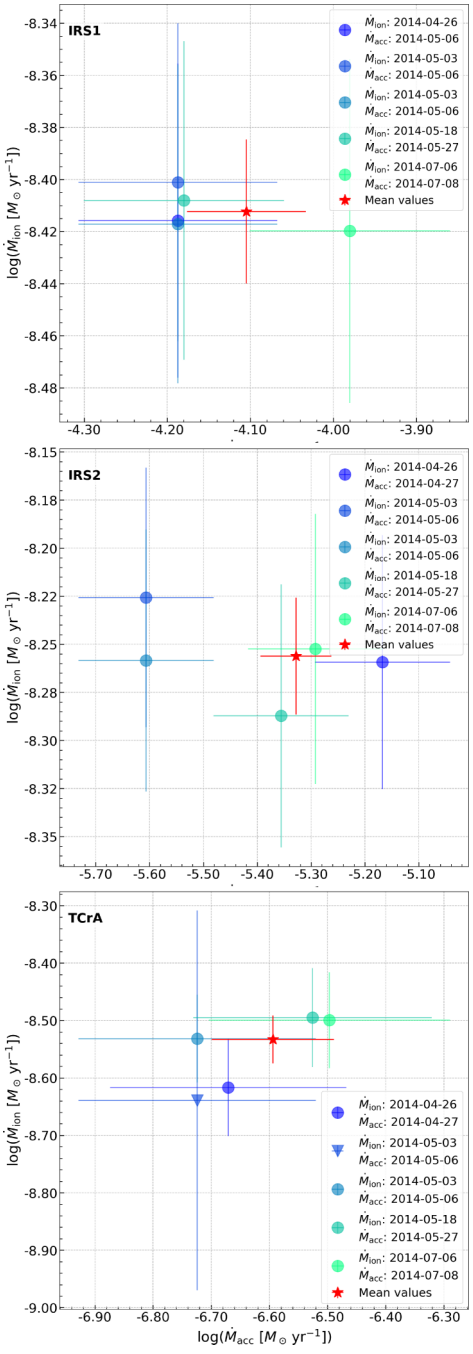

Figure 2. Temporal evolution of individual measurements of $\dot{M}_{acc}$ and $\dot{M}_{ion}$ for the two class I (IRS1, IRS2, top and middle panels) and one class II YSO (TCrA, bottom) with Brγ in emission and VLA detection in individual epochs. CrA43 was excluded due to its unphysically large ejection rate compared to its accretion rate (see Section 4.3). The blue and green points refer to values around the individual epochs marked in the plot legends, whereas the red star is the mean value.

our case, the free–free emission is only sensitive to the ionized component of the ejected material, ξ_{ion}, not to the neutral atomic (B. Nisini et al. 2018) or molecular (T. P. Ray et al. 2023) components. The ξ_{ion} values in our sample are consistent with those reported by A. A. Rota et al. (2024, 2025), who also used the free–free continuum for a sample of class II YSOs mostly located in the Taurus star formation region. Our ξ_{ion} values are also consistent with those of B. Nisini et al. (2018). However, their ejection rates were derived from the high velocity component of the [O I] line in a sample of 131 class II YSOs in several star forming regions. A. A. Rota et al. (2025) showed that, although full discs (FDs) typically accrete at higher rates than transition discs (TDs), the accretion-wind scaling is shallower in TDs, implying a reduced apparent efficiency. The four sources for which we could perform the full analysis are two class IIs and, for the first time, two class I YSOs.

Several reports of rings and gaps in class I discs have been presented (e.g. P. D. Sheehan et al. 2020; C.-H. Hsieh et al. 2024), but the details of mass transport in the discs of embedded YSOs are far from understood. In class II YSOs, studies on magneto-centrifugal launching models have shown that ξ is inversely proportional to the magnetic lever arm λ^{-1} (G. Pelletier & R. E. Pudritz 1992; L. Hartmann et al. 2016; I. Pascucci et al. 2023). This implies that lower ξ values correspond to larger λ, thus resulting in more compact jet launching regions. The lower ξ_{ion} values for class I YSOs in our sample may therefore point to narrower launching zones or different magnetic field morphologies, a scenario pointed out by B. Nisini et al. (2018).

On the other hand, protostellar jets are known to have a nested structure, consisting of high-velocity ionized winds enclosed by layers of atomic and molecular jets with decreasing velocity gradients (e.g. B. Nisini et al. 2024; F. Bacciotti et al. 2025). Therefore, another possible interpretation of the trend shown in Fig. 4 considers the chemical and ionization state of the ejected material, which can be either atomic ionised, atomic neutral, or molecular[5]. A full account of the efficiency of ejected to accreted material should consider these three states, i.e. $\xi_{tot} = \xi_{ion} + \xi_{ato} + \xi_{mol}$ (e.g. R. Fedriani et al. 2019). Assuming that ξ_{tot} remains constant across YSO evolutionary stages, the observed decrease in ξ_{ion} with evolutionary stage suggests that jets are predominantly neutral (atomic and molecular) in the earlier protostellar phases, with the ionization fraction increasing as the YSOs evolve. This scenario is supported by previous studies of Herbig-Haro objects HH 34 (B. Nisini et al. 2016) and HH 211 (T. P. Ray et al. 2023).

4.2 Accretion and ejection variability

Regarding the short-term (days to months) time evolution shown in Fig. 2, there is no clear evidence of a temporal correlation between accretion and ionised mass-loss rates. This can be understood by considering the time-scale of the formation of lobes of ionized gas in the jet, which we approximate as $\sim 0.5 \times$ beamsize divided by the jet velocity, or $\sim 10^2$ d. M. S. Connelley & T. P. Greene (2014) reported the variability of near-IR tracers of accretion and winds in a sample of class I YSOs with a four year survey. They concluded that both types of tracers are sometimes positively or negatively correlated and sometimes uncorrelated, depending on the target. Similar results were obtained by L. E. Ellerbroek et al. (2014) in the Herbig Ae/Be star HD 163 296 and by J. Forbrich et al. (2015) in LRLL 54361. Also, the class 0 YSO HOPS 383, which presented a $\times 35$ increment in bolometric luminosity between 2004 and 2006 (E. J. Safron et al. 2015), did not present a corresponding increase in the centimetre flux of the associated radio jet (R. Galván-Madrid et al. 2015). All these results highlight the complexity of the physical relationship between accretion and ejection in jets and winds (see e.g. M. M. Romanova et al. 2018; Z. Zhu 2025, for detailed simulations).

[5]For simplicity, we neglect the contribution of ionised molecular species.

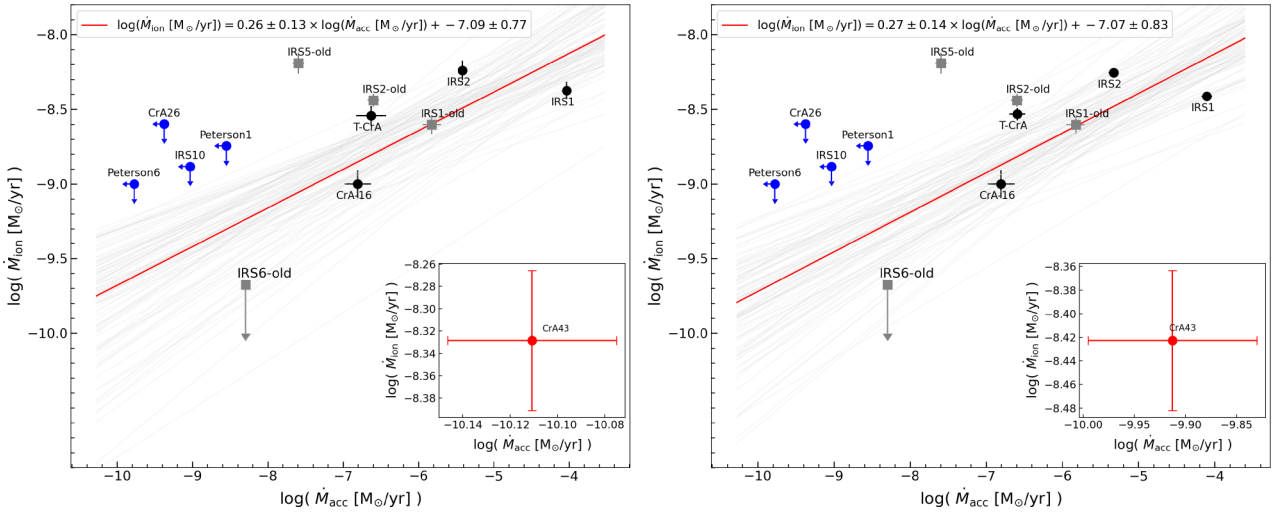

Figure 3. Correlation between the logarithm of the mass accretion rate and the logarithm of the ionized mass-loss rate, including the data from IRS1, IRS2, CrA16, TCrA, Peterson 1, Peterson 6, and CrA 26, but excluding CrA43 (inset) from the fit. We present two fitting scenarios: in the left panel the fit is obtained utilizing the averaged Brγ spectra and epoch-concatenated VLA image; in the right panel, the fit is obtained from averaging the near-simultaneous measurements shown in Fig. 2 for the detections, and upper limits as described in the text. The light grey lines show regression relations drawn from posterior samples restricted to the central 68 per cent credible interval of the slope; the red line indicates the posterior median. The overplotted gray squares, marked with the suffix '-old', show previous measurements obtained from H. B. Liu et al. (2014) and B. Nisini et al. (2005a).

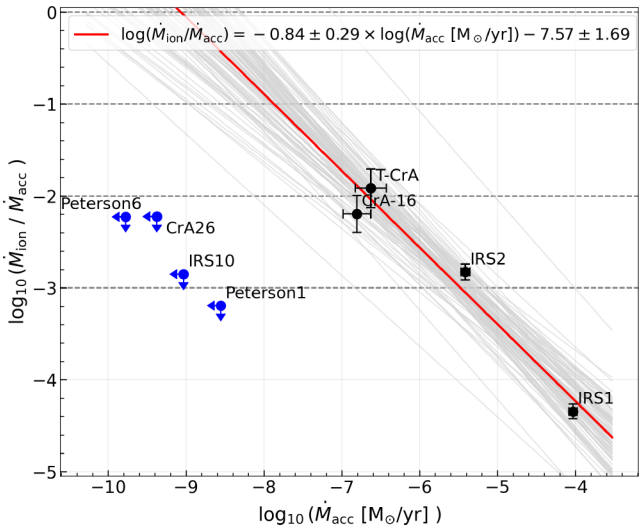

Figure 4. Logarithm of the ratio of the ionised mass-loss rate to the mass-accretion rate, as a function of the latter. The horizontal lines mark efficiency factors $\xi_{\rm ion} = 0.001$, 0.01, 0.1, and 1. The red and grey lines are defined as in Fig. 2.

The observed variability in accretion and ionised mass-loss rates in Fig. 2 is probably due to the inherent stochasticity in these processes (W. J. Fischer et al. 2023).

4.3 Outliers and complex behaviour

The class I YSO CrA43 was excluded from further analysis due to its inferred $\dot{M}_{\rm ion}$ being two orders of magnitude larger than the corresponding $\dot{M}_{\rm acc}$ (see inset plot of Fig. 3). We consider the possible explanation for this anomaly. The KMOS observations were taken during a state of quiescence. During such an episode of a lower accretion rate, the radio jet core could also become optically thin, allowing non-thermal radio emission from the magnetosphere, if present, to reach the observer (e.g. H. B. Liu et al. 2014). More generally, variability in both accretion (e.g. G. Costigan et al. 2014; R. A. B. Claes et al. 2022) and jet ejection (e.g. B. Reipurth et al. 2002; M. Takami et al. 2023) could be an important source of the observed scatter and outliers in studies like the one presented in this paper, even if we attempted to perform observations as simultaneously as possible.

5 CONCLUSIONS

Using multi-epoch coordinated observations with KMOS-VLT and the VLA, we have measured the Brγ line and 3.3 cm radio continuum emission for 26 YSOs in the Coronet cluster. Accretion and ionized jet ejection rates were derived from both tracers for 4 YSOs with confirmed detections, while upper limits were obtained for an additional 4 YSOs. Using time-averaged measurements, we find a sub-linear relation between $\dot{M}_{\rm acc}$ and $\dot{M}_{\rm ion}$, with a slope of $\approx 0.3 \pm 0.1$ in logarithmic space. This implies that the amount of ionized jet ejection follows that of mass accretion across the protostar to protoplanetary disc evolutionary timescales of up to a few Myr. However, we do not find a clear relationship between these quantities in our time monitoring sampling time-scales from days to months, possibly due to the complex interplay between magnetospheric accretion and jet launching processes.

ACKNOWLEDGEMENTS

Based on observations collected at the European Organisation for Astronomical Research in the Southern Hemisphere under ESO programme 093.C-0657. The National Radio Astronomy Observatory is a facility of the National Science Foundation operated under cooperative agreement by Associated Universities, Inc. AG, RGM, JRA, and CCG acknowledge support from CONAHCyT Ciencia de Frontera project ID 86372 'Citlalcóatl'. These authors also thank the support from DGAPA–UNAM and UNAMPAPIIT projects IN105225 and IG101224. RGM acknowledges support from the ESO Scientific Visitor Programme. H.B.L. is sup-

ported by the National Science and Technology Council (NSTC) of Taiwan (Grant Nos. 111-2112-M-110-022-MY3, 113-2112-M-110-022-MY3). The authors thank Stefan Meingast for providing VISIONS photometric data. This research has made use of the following software: ASTROPY (Astropy Collaboration 2018, 2022), and CASA (CASA Team 2022).

DATA AVAILABILITY

The data underlying this article are available in its online supplementary material.

REFERENCES

Adams F. C., Lada C. J., Shu F. H., 1987, ApJ, 312, 788
Alcalá J. M. et al., 2017, A&A, 600, A20
Andre P., 1987, in Montmerle T., Bertout C. eds, Protostars and Molecular Clouds. p. 143
Andre P., Ward-Thompson D., Barsony M., 1993, ApJ, 406, 122
Anglada G., Rodríguez L. F., Carrasco-González C., 2018, A&A Rev., 26, 3
Armitage P. J., Clarke C. J., Palla F., 2003, MNRAS, 342, 1139
Astropy Collaboration, 2018, AJ, 156, 123
Astropy Collaboration, 2022, ApJ, 935, 167
Bacciotti F. et al., , 2025, A&A, 704, 28
Banzatti A., Pascucci I., Edwards S., Fang M., Gorti U., Flock M., 2019, ApJ, 870, 76
CASA Team, 2022, PASP, 134, 114501
Calvet N., Gullbring E., 1998, ApJ, 509, 802
Cazzoletti P. et al., 2019, A&A, 626, A11
Choi M., Hamaguchi K., Lee J.-E., Tatematsu K., 2008, ApJ, 687, 406
Claes R. A. B. et al., 2022, A&A, 664, L7
Connelley M. S., Greene T. P., 2014, AJ, 147, 125
Contreras Peña C. et al., 2017, MNRAS, 465, 3039
Costigan G., Vink J. S., Scholz A., Ray T., Testi L., 2014, MNRAS, 440, 3444
Davies R. I. et al., 2013, A&A, 558, A56
Deller A. T., Forbrich J., Loinard L., 2013, A&A, 552, A51
Dong R., Najita J. R., Brittain S., 2018, ApJ, 862, 103
Dunham M. M. et al., 2014, in Beuther H., Klessen R. S., Dullemond C. P., Henning T., eds, Protostars and Planets VI. Univ. Arizona Press, Tucson, p. 195
Dzib S. A., Loinard L., Ortiz-León G. N., Rodríguez L. F., Galli P. A. B., 2018, ApJ, 867, 151
Ellerbroek L. E. et al., 2014, A&A, 563, A87
Fang M. et al., 2018, ApJ, 868, 28
Fedriani R. et al., 2019, Nat. Commun., 10, 3630
Feigelson E. D., Montmerle T., 1999, ARA&A, 37, 363
Fiorellino E., Tychoniec Ł., Cruz-Sáenz de Miera F., Antoniucci S., Kóspál Á., Manara C. F., Nisini B., Rosotti G., 2023, ApJ, 944, 135
Fiorellino E. et al., 2021, A&A, 650, A43
Fischer W. J., Hillenbrand L. A., Herczeg G. J., Johnstone D., Kospal A., Dunham M. M., 2023, in Inutsuka S., Aikawa Y., Muto T., Tomida K., Tamura M., eds, ASP Conf. Ser. Vol. 534, Protostars and Planets VII. Astron. Soc. Pac., San Francisco, p. 355
Folha D. F. M., Emerson J. P., 2001, A&A, 365, 90
Forbrich J., Preibisch T., 2007, A&A, 475, 959
Forbrich J. et al., 2007, A&A, 464, 1003
Forbrich J., Rodríguez L. F., Palau A., Zapata L. A., Muzerolle J., Gutermuth R. A., 2015, ApJ, 814, 15
Forbrich J., Dzib S. A., Reid M. J., Menten K. M., 2021, ApJ, 906, 23
Frank A. et al., 2014, in Beuther H., Klessen R. S., Dullemond C. P., Henning T., eds, Protostars and Planets VI. Univ. Arizona Press, Tucson, p.451
Freudling W., Romaniello M., Bramich D. M., Ballester P., Forchi V., García-Dabló C. E., Moehler S., Neeser M. J., 2013, A&A, 559, A96
Gaidos E., Gehrig L., Güdel M., 2025, A&A, 696, A207
Galli P. A. B., Bouy H., Olivares J., Miret-Roig N., Sarro L. M., Barrado D., Berihuete A., Brandner W., 2020, A&A, 634, A98
Galván-Madrid R. et al., 2014, A&A, 570, L9
Galván-Madrid R., Rodríguez L. F., Liu H. B., Costigan G., Palau A., Zapata L. A., Loinard L., 2015, ApJ, 806, L32
Garufi A. et al., 2025, A&A, 694, A290
Guo Z. et al., 2020, MNRAS, 492, 294
Hartigan P., Edwards S., Ghandour L., 1995, ApJ, 452, 736
Hartmann L., Herczeg G., Calvet N., 2016, ARA&A, 54, 135
Hsieh C.-H., Arce H. G., Maureira M. J., Pineda J. E., Segura-Cox D., Mardones D., Dunham M. M., Arun A., 2024, ApJ, 973, 138
Liu H. B. et al., 2014, ApJ, 780, 155
Lora V., Nony T., Esquivel A., Galván-Madrid R., 2024, ApJ, 962, 66
Macías E. et al., 2016, ApJ, 829, 1
Manara C. F., Ansdell M., Rosotti G. P., Hughes A. M., Armitage P. J., Lodato G., Williams J. P., 2023, in Inutsuka S., Aikawa Y., Muto T., Tomida K., Tamura M., eds, ASP Conf. Ser. Vol. 534, Protostars and Planets VII. Astron. Soc. Pac., San Francisco, p. 539
Meingast S. et al., 2023, A&A, 673, A58
Miettinen O., Kontinen S., Harju J., Higdon J. L., 2008, A&A, 486, 799
Morales-Calderón M. et al., 2011, ApJ, 733, 50
Muzerolle J., Calvet N., Hartmann L., 2001, ApJ, 550, 944
Myers P. C., 2009, ApJ, 700, 1609
Nisini B., Antoniucci S., Giannini T., Lorenzetti D., 2005a, A&A, 429, 543
Nisini B., Antoniucci S., Giannini T., Lorenzetti D., 2005b, A&A, 429, 543
Nisini B., Giannini T., Antoniucci S., Alcalá J. M., Bacciotti F., Podio L., 2016, A&A, 595, A76
Nisini B., Antoniucci S., Alcalá J. M., Giannini T., Manara C. F., Natta A., Fedele D., Biazzo K., 2018, A&A, 609, A87
Nisini B. et al., 2024, ApJ, 967, 168
Pascucci I., Ricci L., Gorti U., Hollenbach D., Hendler N. P., Brooks K. J., Contreras Y., 2014, ApJ, 795, 1
Pascucci I., Cabrit S., Edwards S., Gorti U., Gressel O., Suzuki T. K., 2023, in Inutsuka S., Aikawa Y., Muto T., Tomida K., Tamura M., eds, ASP Conf. Ser. Vol. 534, Protostars and Planets VII. Astron. Soc. Pac., San Francisco, p. 567
Pelletier G., Pudritz R. E., 1992, ApJ, 394, 117
Peterson D. E. et al., 2011, ApJS, 194, 43
Pudritz R. E., Ouyed R., Fendt C., Brandenburg A., 2007, in Reipurth B., Jewitt D., Keil K., eds, Protostars and Planets V. Univ. Arizona Press, Arizona, p. 277
Ray T. P. et al., 2023, Nature, 622, 48
Reipurth B., Rodríguez L. F., Anglada G., Bally J., 2002, AJ, 124, 1045
Robitaille T. P., Whitney B. A., Indebetouw R., Wood K., 2007, ApJS, 169, 328
Rodríguez L. F., Zapata L. A., Dzib S. A., Ortiz-León G. N., Loinard L., Macías E., Anglada G., 2014, ApJ, 793, L21
Romanova M. M., Blinova A. A., Ustyugova G. V., Koldoba A. V., Lovelace R. V. E., 2018, New A, 62, 94
Rota A. A., Meijerhof J. D., van der Marel N., Francis L., van der Tak F. F. S., Sellek A. D., 2024, A&A, 684, A134
Rota A. A. et al., , 2025, A&A, 700, 11
Safron E. J. et al., 2015, ApJ, 800, L5
Sharples R. et al., 2013, The Messenger, 151, 21
Sheehan P. D., Tobin J. J., Federman S., Megeath S. T., Looney L. W., 2020, ApJ, 902, 141
Shu F., Najita J., Ostriker E., Wilkin F., Ruden S., Lizano S., 1994, ApJ, 429, 781
Sicilia-Aguilar A., Henning T., Juhász A., Bouwman J., Garmire G., Garmire A., 2008, ApJ, 687, 1145
Sicilia-Aguilar A., Henning T., Kainulainen J., Roccatagliata V., 2011, ApJ, 736, 137
Skrutskie M. F. et al., 2006, AJ, 131, 1163
Takami M. et al., 2006, ApJ, 641, 357
Takami M. et al., 2020, ApJ, 901, 24
Takami M. et al., 2023, ApJS, 264, 1
Testi L. et al., 2025, A&A, 703, A277
Tychoniec Ł. et al., 2018, ApJS, 238, 19

Williams J. P., Cieza L. A., 2011, ARA&A, 49, 67
Zhu Z., 2025, MNRAS, 537, 3701

SUPPORTING INFORMATION

Supplementary data are available at *MNRAS* online.

suppl_data

Please note: Oxford University Press is not responsible for the content or functionality of any supporting materials supplied by the authors. Any queries (other than missing material) should be directed to the corresponding author for the article.

This paper has been typeset from a TEX/LATEX file prepared by the author.